


 Cite this: *RSC Adv.*, 2026, 16, 1833

# A simple approach to fabricate a highly-sensitive lead(II) ion electrochemical sensor based on plate-shaped Cu-BTC and particle-shaped Fe-BTC

 Tuyet Nhung Pham,<sup>a</sup> Nguyen Le Nhat Trang,<sup>a</sup> Ong Van Hoang,<sup>ab</sup> Tien Van Manh,<sup>c</sup> Nguyen Quang Hoa,<sup>d</sup> Vu Dinh Lam,<sup>e</sup> Manh-Huong Phan<sup>f</sup> and Anh-Tuan Le<sup>a\*</sup>

A challenging task is to study and improve the electrochemical behaviors and sensing performance of Fe-BTC and Cu-BTC-based electrodes for sensitive detection toward lead(II) ions ( $\text{Pb}^{2+}$ ). In the present work, particle-shaped Fe-BTC was effectively decorated on the plate-like Cu-BTC substrate to form a 3D-composite architecture using the microwave-assisted electrochemical method and successfully detected  $\text{Pb}^{2+}$  ions for the first time. This hierarchical structure served as a promising candidate for modifying the working electrode surface, facilitating favorably the electrochemical reaction of  $\text{Pb}^{2+}$  ions. The structural and morphological characteristics were thoroughly investigated using scanning electron microscopy (SEM) and X-ray diffraction (XRD), confirming the successful integration of Fe-BTC and Cu-BTC phases. Interestingly, the Fe-BTC@Cu-BTC-modified screen-printed electrode (SPE) exhibited several advantageous features, including enhanced electrical conductivity, increased electroactive surface area, and superior electron transfer kinetics. Consequently, the Fe-BTC@Cu-BTC/SPE demonstrated a low overpotential for  $\text{Pb}^{2+}$  oxidation, a wide linear detection range, low limit of detection (LOD), high sensitivity, and excellent selectivity. Its practical applicability was further validated through successful  $\text{Pb}^{2+}$  detection in shampoo samples. Besides, this study provided useful insights into the nature of the enhancement from effective integration between geometric configuration and compositional integration of Fe-BTC and Cu-BTC materials to guide the design of suitable metal-organic framework (MOF) structures for high-performance electrochemical sensing and related applications.

 Received 17th November 2025  
 Accepted 23rd December 2025

DOI: 10.1039/d5ra08888g

[rsc.li/rsc-advances](https://rsc.li/rsc-advances)

## 1. Introduction

Metal-organic frameworks (MOFs) are considered a unique class of functional inorganic-organic hybrid materials, characterized by their rationally designed architectures and uniform empty spaces (pores and cavities) at the nanoscale. A large number of various MOF structures have been reported, confirming extremely high surface area and pore volume, flexible framework, tunable porous structure, unsaturated metal sites,

and inherent non-toxicity. These attributes often surpass those of conventional porous materials, including carbonaceous compounds, metal phosphates, and zeolites.<sup>1-5</sup> Among the diverse MOF families, Cu-BTC (also known as HKUST-1) and Fe-BTC have emerged as particularly important due to their microporous frameworks and unique physicochemical characteristics. These include large specific surface area, high pore volume, high chemical stability, strong Lewis acidity based on the high content of open metal sites, and labile coordinated water molecules. As a result, Fe-BTC and Cu-BTC MOFs have been widely explored for many different applications, such as energy storage, catalysis, sensing, adsorption, and biomedical materials.<sup>5-8</sup>

The topological nature of MOFs is defined by the ordered arrangement of the blocks between ligands (long organic molecule chains) and metal nodes. Typically, MOFs are synthesized by heating metal ions and organic linkers in suitable solvents over several hours or days. Post-synthesis, vacuum treatment is often employed to remove residual solvent molecules trapped within the porous network. Achieving high-quality MOFs requires precise control over synthesis

<sup>a</sup>Phenikaa University Nano Institute (PHENA), Phenikaa School of Engineering (PSE), Phenikaa University, Hanoi 12116, Vietnam. E-mail: [nhung.phamthituyet@phenikaa-uni.edu.vn](mailto:nhung.phamthituyet@phenikaa-uni.edu.vn); [tuan.leanh@phenikaa-uni.edu.vn](mailto:tuan.leanh@phenikaa-uni.edu.vn)

<sup>b</sup>University of Transport Technology, Trieu Khuc, Thanh Xuan District, Hanoi, Vietnam  
<sup>c</sup>Research Group on Smart Materials & Tech. Application (SM&A), University of Transport Technology, Trieu Khuc, Thanh Liet, Hanoi 100000, Vietnam

<sup>d</sup>Faculty of Physics, VNU University of Science, Vietnam National University, Hanoi, Thanh Xuan, Hanoi, Vietnam

<sup>e</sup>Graduate University of Science and Technology (GUST), Institute of Physics, Vietnam Academy of Science and Technology, Hanoi 10000, Vietnam

<sup>f</sup>Center for Materials Innovation and Technology (CMIT), VinUniversity, Gia Lam District, Hanoi 10000, Vietnam



parameters, including the choice of metal precursors, ligands, solvents, and temperature.<sup>9</sup> Some various synthetic strategies have been developed to fabricate MOFs, for example, the solvo/hydrothermal method, solvothermal synthesis, electrochemical methods, mechanochemical synthesis, spray-drying, and microwave-assisted techniques.<sup>10,11</sup> Due to the structural complexity and sensitivity of MOF formation to reaction conditions-including temperature, pH, solvent type, and kinetic or thermodynamic factors-these parameters critically influence the resulting material properties. To create Fe-BTC, Cu-BTC, and Fe-BTC@Cu-BTC composite structures with high yields and purity, in this research, the microwave-assisted electrochemical synthesis has been first proposed as a low cost, facile, efficient, and fast method because of its shorter reaction time, uniform and rapid heating rate, faster kinetics, higher phase purity, higher yield, and better reliability and reproducibility than other conventional methods.<sup>5,10,12</sup>

Investigation of the applicability of the Cu-BTC MOF structures in electrochemical sensors has been extensively explored in recent years.<sup>1-3,6,13,14</sup> For example, N. Zalpour *et al.*<sup>11</sup> successfully synthesized an ultrathin Cu-BTC layer directly on a glassy carbon electrode (GCE) using a molecularly imprinted polymer (MIP) technique. Thanks to this unique hybridization, Cu-BTC/MIPs structure functioned as a super-adsorbent with very high selectivity, sensitivity, porosity, and special recognition sites for pregabalin (PGB) ultra-trace. The resulting GCE/Cu-BTC sensor demonstrated a remarkable linear detection range from 0.05–800 pM, corresponding a limit of detection (LOD) of 0.9 fM. More recently, Cu-BTC-based sensors have been applied for the sensitive detection of lead(II) ions (Pb<sup>2+</sup>).<sup>13,15</sup> G. A. Bodkhe *et al.*<sup>15</sup> successfully developed a novel composite material by incorporating gold nanoparticles (Au NPs) into the Cu-BTC framework. The synergistic effect between the high surface area of Cu-BTC and the excellent electrocatalytic activity of Au NPs enabled a highly sensitive and selective electrochemical response toward Pb<sup>2+</sup>, achieving detection limits as low as 1 nM. Beyond heavy metal detection, Cu-BTC MOF-based electrodes have also been employed for the electrochemical determination of various analytes, including sunset yellow/tartrazine,<sup>1</sup> hydroquinone/catechol,<sup>16</sup> and ammonia.<sup>17</sup> Similar to Cu-BTC, the utilization of Fe-BTC MOF for electrochemical sensors has attracted significant attention under the inspiration of the above fascinating properties.<sup>7,8</sup> Nevertheless, challenges such as poor crystallinity, limited electrical conductivity, and structural instability have hindered their direct use in sensor development.<sup>2,6</sup> To overcome these limitations, researchers have focused on developing Fe-BTC-based composites and derivatives to enhance electrode stability and repeatability.<sup>18</sup> M. C. Maridevaru *et al.*<sup>8</sup> reported that the utilization of Fe-MOF nanotextures for identifying bisphenol A (BPA) achieved impressive results arising from the excellent guest interaction potential of organic ligands and the substantial surface area of metal. Fe-MOF-modified electrode displayed a linear sensitivity in the range from 0.1 μM to 15 μM with an LOD of 0.1 μM, along with excellent recovery and stable performance over a one-month period. More recently, the number of studies on bimetallic organic framework (BMOF),

such as Cu/FeBTC has increased gradually. W. Y. Siew *et al.*,<sup>19</sup> reported a one-pot green synthesis method for the incorporation of Fe<sup>2+</sup> into CuBTC at room temperature. This approach was aimed at modifying the surface morphology and pore formation *via* the synergistic effect of the second metal ions. As a result, the BET surface area was enhanced from 709 m<sup>2</sup> g<sup>-1</sup> to 1240 m<sup>2</sup> g<sup>-1</sup>, and the adsorption capacity for methylene blue increased approximately six times compared to that of CuBTC alone. Another study, W. Xiang *et al.*<sup>20</sup> demonstrated the effective removal of tetracycline antibiotics from aquatic environments using Fe/CuBTC composites. By optimizing the Fe/Cu molar ratio to 1:2, the void ratio of Fe/Cu-MOFs increased to 0.7326 cm<sup>3</sup> g<sup>-1</sup>, with the maximum tetracycline (TC) adsorption capacity for Fe/CuBTC-1/2 reported at  $Q_{\max} = 1130.23$  mg g<sup>-1</sup>.

Unfortunately, to the best of our knowledge, no report on how the effective integration of two distinct MOF materials, specifically Fe-BTC and Cu-BTC MOFs into a hierarchical 3D-composite architecture, and how the electrodes modified with these MOF structures improve the electrochemical behaviors and sensing performance toward Pb<sup>2+</sup> detection, has been reported. Despite the fact that these MOF-based electrodes have been explored for detecting various target analytes, there remains a notable gap in comparative investigations and mechanistic explanations regarding the observed enhancements in performance, particularly for Pb<sup>2+</sup> sensing. This research gap is of significant interest, especially given the growing application of MOF-based composites and derivatives in electrochemical sensor development. The selection of Cu-BTC and Fe-BTC in this work is motivated by both the structural differences in their framework regularity and their broad applicability in electrochemical sensing. A facile, cost-effective microwave-assisted electrochemical method was used for the first time to prepare Fe-BTC, Cu-BTC, and Fe-BTC@Cu-BTC composite. In addition to the fundamental knowledge, a comprehensive comparative analysis of their electrochemical characteristics and sensing performance was conducted. This includes the evaluation of key kinetic parameters to elucidate the role of structural integration in enhancing sensor functionality. The findings aim to provide both fundamental insights and practical guidance for the rational design of MOF-based materials in advanced electrochemical applications.

## 2. Experimental

### 2.1. Material

Trimesic acid (H<sub>3</sub>BTC, >95%), potassium chloride (KCl), potassium ferricyanide (K<sub>3</sub>[Fe(CN)<sub>6</sub>]), and potassium ferrocyanide trihydrate (K<sub>4</sub>[Fe(CN)<sub>6</sub>]·3H<sub>2</sub>O) were obtained from Sigma-Aldrich (USA) and Merck KGaA (Germany). *N,N*-Dimethylformamide (DMF), sodium chloride (NaCl), and ethanol were purchased from Xilong Scientific Co., Ltd (China) and Guangdong Guanghua Sci-Tech Co (China). Sodium acetate (NaAc), acetic acid (HAc), HCl, NaOH were purchased from Shanghai Chemical Reagent to prepare acetate buffer solution (AcB, 0.1 M) as supporting electrolyte. Pb<sup>2+</sup> standard aqueous solution was prepared and diluted from stock solution of PbCl<sub>2</sub> (Sigma-Aldrich (USA)). All chemicals utilized without any



further purification. Besides, the commercial carbon screen-printed electrode (SPE-DS110) was supplied by DS Dropsens, Spain.

## 2.2. Method

**2.2.1. Preparation of Fe-BTC and Cu-BTC by microwave-assisted electrochemical method.** Unlike conventional approaches, electrochemical synthesis involves the anodic dissolution of elemental metal plates, which subsequently react with organic ligands present in the electrolyte to produce the desired metal-organic framework (MOF). Additionally, microwave-assisted heating enhances the nucleation and crystal rate of MOFs due to uniform thermal distribution. This method enables efficient and rapid MOF formation with superior quality, yielding large quantities of homogeneous micro- and nanocrystals with controlled size and morphology within a short time frame.

In this study, Fe-BTC and Cu-BTC structures were synthesized using a microwave-assisted electrochemical method. Initially, 0.585 g of NaCl was dissolved in 200 mL distilled water, and the solution was magnetically stirred for 30 minutes at room temperature to prepare the electrolyte solution. For Fe-BTC synthesis, two iron bars were arranged in parallel inside a 250 mL glass beaker on a magnetic stirrer, serving as sacrificial anode and cathode. A direct current (DC) potential of 8 V was applied to the iron bars for 2 hours under continuous stirring at room temperature. After the electrochemical reaction, 2.1 g of trimesic acid ( $H_3BTC$ ) was introduced into the solution, and stirring was continued for an additional 2 hours to ensure homogeneity. Herein, the applied electric field facilitated electron loss in metallic Fe, leading to  $Fe^{3+}$  cation formation, which subsequently coordinated with BTC ligands in the solvent to yield a precipitate. The reaction mixture was then subjected to microwave heating at 80 °C for 10 minutes using a power of 500 W. The resulting precipitate was collected by centrifugation, followed by filtration and sequential washing with dimethylformamide (DMF), ethanol, and distilled water. Finally, the purified product was dried at 60 °C in air for 12 hours. The synthesis of Cu-BTC MOF material was carried out using the same procedure.

**2.2.2. Preparation of the Fe-BTC@Cu-BTC by microwave-assisted electrochemical method.** The Fe-BTC@Cu-BTC composites was also synthesized using a microwave-assisted electrochemical method. A higher proportion of Cu in the composite (1:3 ratio) was used. The rationale behind this choice was that Cu-BTC offers better electrical conductivity and crystal structure, while the low Fe-BTC crystalline structure contributes significantly to the adsorption capacity. A higher proportion of Cu in the composite (1:3 ratio) was expected to enhance electron transfer kinetics without compromising the structural integrity and stability. To begin, a homogeneous mixture was prepared by combining 50 mL of  $Fe^{3+}$  ion solution and 150 mL of  $Cu^{2+}$  ion solution, obtained from the previously described electrochemical synthesis processes. Subsequently, 2.1 g of  $H_3BTC$  was added to the mixture and stirred for 2 hours to ensure uniformity and complete reaction between the metal

ions and organic ligands. The reaction mixture was then subjected to microwave heating at 80 °C for 10 minutes using a power of 500 W. The resulting precipitate was collected *via* centrifugation, followed by filtration and sequential washing with dimethylformamide (DMF), ethanol, and distilled water, respectively. Finally, the purified precipitate was dried at 60 °C for 12 hours in air to obtain the Fe-BTC@Cu-BTC composites.

**2.2.3. Preparation modified SPEs.** For the electrode surface modification process, Fe-BTC, Cu-BTC, and Fe-BTC@Cu-BTC was carried out in sequential steps. Prior to surface modification, commercial SPE electrodes were cleaned using ethanol and water, then dried in air at room temperature. For the preparation of the Fe-BTC/SPE electrode, 2.0 mg of Fe-BTC sample was dispersed in 2.0 mL of distilled water and subjected to ultrasonic treatment for 30 min to obtain a homogeneous Fe-BTC suspension at a concentration of 1.0 mg mL<sup>-1</sup>. The working electrode surface of the SPE was then modified by carefully dropping the suspension drop by drop until a total volume of 6.0 μL was reached (drop-casting technique). Finally, the Fe-BTC-modified electrode was dried at 40 °C for 3 hours in air. The same procedure was followed for the Cu-BTC-modified electrode and Fe-BTC@Cu-BTC-modified electrode. Immediately afterward, 6.0 μL of this suspension was carefully dropped onto the bare SPE surface and allowed to dry under ambient conditions.

**2.2.4. Real samples preparation.** For the preparation of real samples, a commercially available shampoo, purchased from a local supermarket in Hanoi, Vietnam, was utilized for the  $Pb^{2+}$  detection. Initially, 1.0 mL of shampoo sample was added to a beaker containing 8.0 mL of 0.1 M acetate buffer (AcB) solution. The mixture was homogenized *via* a vortex mixer and subsequently subjected to ultrasonic treatment for 15 min. Following this pre-treatment,  $Pb^{2+}$  was introduced into the shampoo samples at varying concentrations (5, 10, 25, and 75 ppb) as standard addition samples for analytical evaluation.

## 2.3. Apparatus

**2.3.1. Physical measurements.** The structural characterization of the synthesized materials was conducted *via* X-ray diffraction (XRD) analysis, utilizing a D8 Advance diffractometer equipped with a LYNXEYE detector. The measurements were performed in Bragg-Brentano geometry, employing Cu-K $\alpha$  radiation with a wavelength of  $\lambda = 1.54056 \text{ \AA}$ . Raman spectra were recorded at a laser Raman spectrometer (Macro-Ram, Raman<sup>TM</sup>) with an excitation wavelength of 785 nm. Furthermore, the surface morphology and spatial distribution of the materials were examined using a field emission scanning electron microscope (FE-SEM, Hitachi S-4800, Japan) and energy dispersive X-ray spectroscopy (EDS, HITACHI).

**2.3.2. Evaluation of electrochemical characterizations.** All electrochemical measurements in this study were conducted using a Palmsens4 electrochemical workstation under ambient conditions. The electrochemical characteristics of both the bare screen-printed electrode (SPE) and modified SPEs were analyzed using cyclic voltammetry (CV) and electrochemical impedance spectroscopy (EIS) in a 0.1 M KCl solution containing 5.0 mM



$K_3[Fe(CN)_6]/K_4[Fe(CN)_6]$ . CV measurements were performed in the potential range of  $-0.3$  to  $0.6$  V and scan rates varying from  $20$  to  $70$   $mV s^{-1}$ . Additionally, EIS measurements were performed using AC potentials across a frequency spectrum spanning  $0.01$  to  $50$  kHz. Furthermore, the electrochemical performance of  $Pb^{2+}$  detection on various modified electrodes was systematically investigated in a  $0.1$  M acetate buffer (AcB) solution using CV and differential pulse anodic stripping voltammetry (DPASV). In this case, CV measurements were carried out at different scan rates ( $20$ – $70$   $mV s^{-1}$ ) within a potential window of  $-1.0$  to  $0.0$  V. Meanwhile, DPASV measurements were tested under specific experimental conditions, including: equilibrium time ( $T_{equilibrium} = 20$  s), step potential ( $E_{step} = 0.006$ ), pulse amplitude ( $E_{pulse} = 0.075$  V), pulse duration ( $T_{pulse} = 0.2$  s), and scan rate of  $15$   $mV s^{-1}$ , respectively.

### 3. Result and discussion

#### 3.1. Microstructure and physical characterizations

Powder X-ray diffraction (XRD) patterns of Cu-BTC, Fe-BTC, and Fe-BTC@Cu-BTC composites synthesized at room temperature are displayed in Fig. 1a. The diffraction profiles confirm the formation of crystalline phases characteristic of metal–organic frameworks (MOFs), as evidenced by sharp and intense peaks in

the synthesized samples. Namely, the well-defined diffraction peaks were located at  $9.3^\circ$ ,  $11.5^\circ$ ,  $13.3^\circ$ ,  $17.39^\circ$ ,  $18.8^\circ$ ,  $21.1^\circ$ ,  $25.6^\circ$ , and  $29^\circ$ , which are corresponding to crystal planes of (220), (222), (400), (333), (440), (620), (731), and (660), indicating the formation of good Cu-BTC crystal structure (a face-centered cubic crystal lattice). Interestingly, XRD analysis indicated that the absence of extraneous peaks further validates the phase purity of the synthesized Cu-BTC. Unlike Cu-BTC, the XRD pattern of Fe-BTC sample shows broad characteristic diffraction peaks of Fe-BTC at approximately  $2\theta = 10.6^\circ$ ,  $18.9^\circ$ ,  $24^\circ$ , and  $27.8^\circ$ , with intensities below  $100$  a.u., exhibiting a low crystalline structure of synthesized Fe-BTC sample. This observation aligns with previous reports that describe Fe-BTC as a semi-amorphous structure.<sup>19,21</sup> Additionally, the co-appearance of some additional peaks of secondary phase as impurity was found at around  $2\theta = 35.5^\circ$ ,  $42.8^\circ$ ,  $53.5^\circ$ ,  $57^\circ$ , and  $62^\circ$ , matching the standard JCPDS file (PDF No. 65-3107) of  $Fe_3O_4$  phase at Fe-BTC sample.<sup>22</sup> An explanation for the phenomenon was that the influence of localized instantaneous high heating in the microwave irradiation process produced local “super hot” dots, facilitating the natural oxidation and aggregation of iron ions to grow and form into the  $Fe_3O_4$  phase on the Fe-BTC surface. This phenomenon has been observed in many previous reports involving the synthesis of  $Fe_3O_4$  crystals using microwave

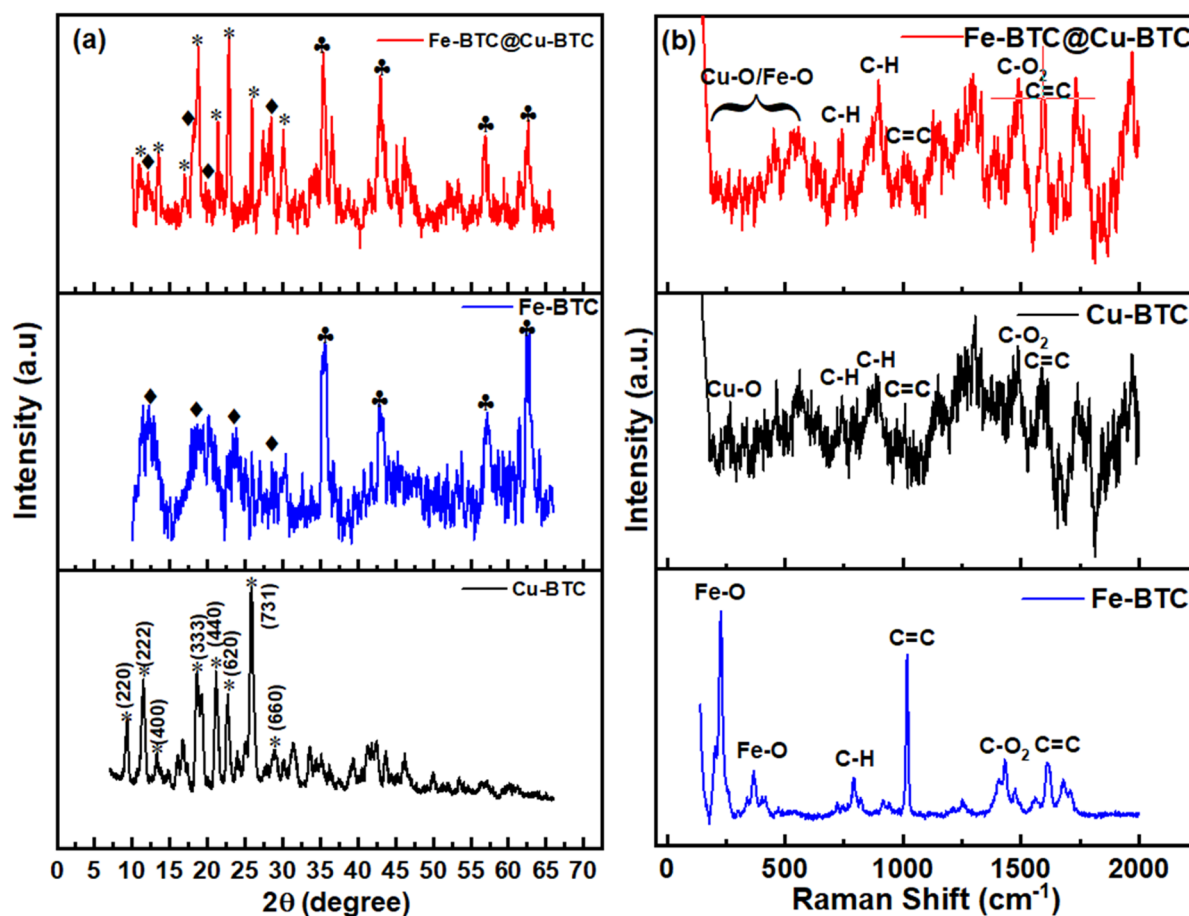


Fig. 1 (a) Powder XRD spectra and (b) Raman spectra obtained at the Cu-BTC, Fe-BTC, and Fe-BTC@Cu-BTC samples.



irradiation.<sup>22–24</sup> More importantly, the XRD pattern of the Fe-BTC@Cu-BTC composite, synthesized with a Fe<sup>2+</sup>/Cu<sup>2+</sup> molar ratio of 1 : 3, retained the characteristic peaks of both parent MOFs without significant structural distortion, while, just had slightly different peak intensity when compared to Cu-BTC and Fe-BTC structures. It was demonstrated that the nature of iron ions tends to form a less crystalline compound with H<sub>3</sub>BTC. Therefore, the co-introducing both two ions Cu<sup>2+</sup> and Fe<sup>3+</sup> into a crystalline MOF structure might be less favourable as Cu<sup>2+</sup> centers combined with the BTC ligand to create a highly crystalline structure. This confirms the successful integration of individual phases (Cu-BTC and Fe-BTC) into a composite material while preserving their crystalline integrity. The coexistence of these phases is expected to contribute positively to the electrochemical performance of the composite electrode.

The structural and bonding characteristics of the synthesized samples were further investigated using Raman spectroscopy, as shown in Fig. 1b. The spectra exhibit distinct bands in the low-frequency region (below 600 cm<sup>-1</sup>), corresponding to vibrations of the coordination bonds between the metal centers (Cu or Fe) and oxygen atoms of the organic framework.<sup>25,26</sup> For the Fe-BTC sample, double peaks observed at 231 and 365 cm<sup>-1</sup> are attributed to Fe–O stretching modes. Similarly, the bands at

261 and 459 cm<sup>-1</sup> correspond to Cu–O stretching vibrations in the Cu-BTC sample. In the higher-frequency region (600–2000 cm<sup>-1</sup>), characteristic bands associated with the BTC ligand were recorded across all three samples. Specifically, peaks at 1011 and 1600 cm<sup>-1</sup> are assigned to C=C stretching modes of the benzene ring, while peaks at 742 and 896 cm<sup>-1</sup> correspond to in-plane bending and out-of-plane C–H bending vibrations, respectively. Additionally, the peak at around 1480 cm<sup>-1</sup> was ascribed to the symmetric stretching modes from the carboxylate groups of BTC, which are labeled as C–O<sub>2</sub>. The presence of these characteristic Raman features confirms the successful synthesis of Cu-BTC, Fe-BTC, and their composite materials, consistent with previously reported results.<sup>1,25–28</sup>

The surface morphology and size of the synthesized materials were examined using scanning electron microscopy (SEM), as illustrated in Fig. 2a. The Cu-BTC sample, prepared *via* a microwave-assisted electrochemical method, exhibited a well-defined plate-like morphology characterized by a smooth and uniform surface, aligning with the well-defined peaks in the XRD patterns for Cu-BTC sample. The good agreement between the SEM images and XRD results demonstrates that the well-shaped crystals observed in SEM originate from a well-crystallized framework, as confirmed by the XRD peak

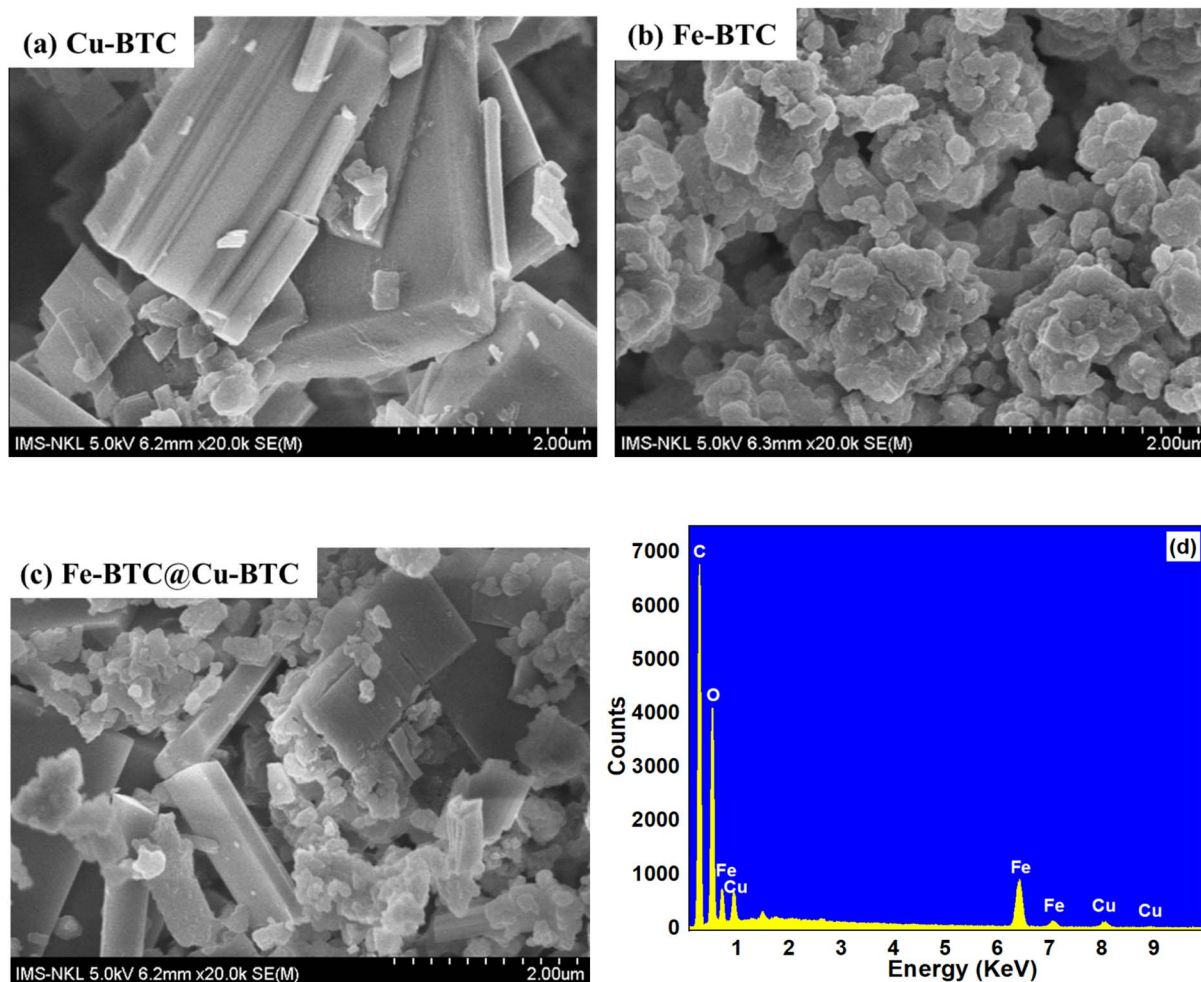


Fig. 2 FESEM images of (a) Cu-BTC, (b) Fe-BTC, (c) Fe-BTC@Cu-BTC samples; and (d) EDS analysis of Fe-BTC@Cu-BTC composites.



sharpness, peak intensity, and phase purity. Although Cu-BTC typically crystallizes in an octahedral form, the utilization of microwave irradiation facilitated rapid and homogeneous heating, which significantly enhanced the nucleation rate and nuclei concentration throughout the solution. This simultaneously accelerated crystal growth process led to the formation of plate-like crystals with an average size of several micrometers, deviating from the conventional octahedral geometry.<sup>5,29</sup> In contrast, the Fe-BTC sample displayed poorly-ordered particle-shaped morphology in which irregular particles aggregated into clusters with an average size of approximately 400–500 nm. This behavior aligns with the weak and broadened diffraction peaks observed in the XRD pattern and may be attributed to surface functional groups that enhance interparticle interactions and hinder well-defined crystal growth. For the Fe-BTC@Cu-BTC composite, SEM analysis revealed a more distinct morphology with reduced particle dimensions. Fe-BTC particles were distributed across the Cu-BTC surface, resulting in a smaller particle size ranging from 200 to 300 nm. Meanwhile, the Cu-BTC plates served as an effective template, enabling homogeneous dispersion of Fe-BTC and minimizing agglomeration. This structural coupling is anticipated to enhance the physicochemical properties of the composite, particularly by increasing the overall surface area and empty space volume within the composite structure. Moreover, the synergistic interaction between the two MOF components promises to improve the depth, transfer, and accessibility of targeted molecules to electroactive sites inside; a powerful tool for fast and efficient electron transport in electrochemical applications.

The elemental composition and distribution of the synthesized samples were examined in detail using energy-dispersive X-ray spectroscopy (EDS) within a selected region. Elemental mapping images confirmed the presence and uniform distribution of the characteristic elements of Cu-BTC and Fe-BTC,

namely Fe, Cu, O, and C (Fig. S1). Quantitative analysis revealed that the Fe-BTC@Cu-BTC composite sample consisted primarily of 15.72% Fe, 3.81% Cu, 46.23% C, and 34.24% O (Fig. 2d). These findings validate the successful synthesis of the individual MOFs and their composite structure.

### 3.2. Electrochemical investigations

CV measurement was performed to first test and evaluate the electrochemical properties of newly developed electrochemical sensors modified with Cu-BTC, Fe-BTC, and Fe-BTC@Cu-BTC. Fig. 3a presents the CV curves recorded for all electrodes in 0.1 M KCl solution containing 5.0 mM  $[\text{Fe}(\text{CN})_6]^{3-/4-}$ . All electrodes exhibited a pair of obvious reversible redox peaks, corresponding to the standard redox reaction of  $[\text{Fe}(\text{CN})_6]^{3-}/[\text{Fe}(\text{CN})_6]^{4-}$  probe. Among the proposed electrodes, the Fe-BTC@Cu-BTC/SPE exhibited the highest reduction response current (261  $\mu\text{A}$ ), followed by Fe-BTC/SPE (224  $\mu\text{A}$ ), Cu-BTC/SPE (194  $\mu\text{A}$ ), and bare SPE (110  $\mu\text{A}$ ). These results clearly indicate that the electrochemical behaviors were considerably improved, particularly at Fe-BTC@Cu-BTC/SPE, which increased by around 2.3-fold compared to bare SPE. To further elucidate the observed enhancement, peak-to-peak potential separation ( $\Delta E_p$ ) was analyzed for each electrode. The following trend was observed: bare SPE (317 mV) > Fe-BTC@Cu-BTC/SPE (306 mV) > Fe-BTC/SPE (258 mV) > Cu-BTC/SPE (218 mV). Given that  $\Delta E_p$  is inversely proportional to electron transfer kinetics, the reduced separation at as-prepared electrodes suggests superior electron transfer efficiency.<sup>30,31</sup> The electrode interface and electronic transmission properties of the proposed electrodes were also investigated in detail *via* electrochemical impedance spectroscopy (EIS) in 5.0 mM  $[\text{Fe}(\text{CN})_6]^{3-/4-}$  aqueous solution containing 0.1 M KCl. It can be inferred from Fig. 3b that modification with MOF structures significantly reduced the semicircle diameter in the high-frequency region of the Nyquist plots, indicating lower charge-transfer resistance ( $R_{ct}$ ). Based on

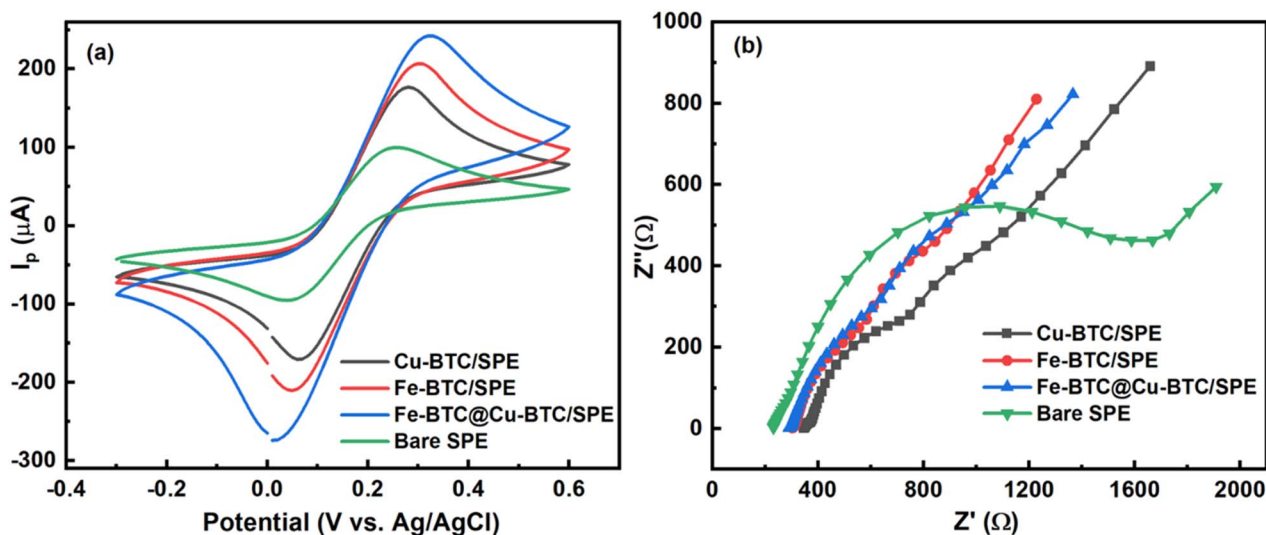


Fig. 3 (a) CV profiles at scan rate  $50 \text{ mV s}^{-1}$  and (b) Nyquist diagrams of EIS in 0.1 M KCl containing 5.0 mM  $[\text{Fe}(\text{CN})_6]^{3-/4-}$  of various proposed electrodes.



fitting with the Randles equivalent circuit, the  $R_{ct}$  values were determined to be 1100  $\Omega$  (bare SPE), 330  $\Omega$  (Cu-BTC/SPE), 216  $\Omega$  (Fe-BTC/SPE), and 117  $\Omega$  (Fe-BTC@Cu-BTC/SPE), confirming enhanced conductivity and interfacial charge transfer.

Afterwards, the effect of the scan rate on the redox response intensity was also investigated *via* CV measurements in the same electrolyte system, with scan rates ranging from 20 to 70  $\text{mV s}^{-1}$ . As described in Fig. 4a–c, the response current ( $I_p$ ) increased with the increase of the scan rate ( $\nu$ ). In addition, the good linear relationship between current ( $I_p$ ) and the square root of scan rate ( $\nu^{1/2}$ ) was observed, obeying the linear regression equations:  $I_{pa}$  ( $\mu\text{A}$ ) =  $18.26\nu^{1/2} + 83.19$  ( $R^2 = 0.998$ ) for Cu-BTC/SPE,  $I_{pa}$  ( $\mu\text{A}$ ) =  $21.36\nu^{1/2} + 83.64$  ( $R^2 = 0.998$ ) for Fe-BTC/SPE, and  $I_{pa}$  ( $\mu\text{A}$ ) =  $22.55\nu^{1/2} + 112.15$  ( $R^2 = 0.999$ ) for Fe-BTC@Cu-BTC/SPE, respectively. This confirmed that the electron transfer reaction of  $\text{Fe}(\text{CN})_6^{3-/4-}$  and mass transport on the proposed electrodes is regulated by a diffusion-controlled mechanism. To determine the electrochemical active area ( $A$ ), the Randles–Sevcik equation at the room conditions (25  $^\circ\text{C}$ ) was used:<sup>31–33</sup>  $I_p$  ( $\mu\text{A}$ ) =  $2.69 \times 10^5 n^{3/2} A D^{1/2} \nu^{1/2} C$ ; where  $n = 1$  (the total number of electrons transferred in redox reaction),  $D = 6.5 \times 10^{-6}$  (diffusion coefficient  $\text{cm}^2 \text{s}^{-1}$ ), and  $C$  is the bulk concentration. According to that, the value of electrochemical active area ( $A$ ) was calculated approximately 0.180  $\text{cm}^2$  for the bare SPE and 0.253, 0.293, and 0.341  $\text{cm}^2$  for the modified electrodes (Cu-BTC/SPE, Fe-BTC/SPE, and Fe-BTC@Cu-BTC/SPE), respectively. From that, the electron transfer rate constant ( $k_{et}$ ) was directly determined using  $R_{ct}$  and  $A$  by the

equation:<sup>31</sup>  $k_{et} = RT/n^2 F^2 A C_0 R_{ct}$ . As expected, considerable increases in  $k_{et}$  values were found around 0.0006, 0.0008, and 0.002 for Cu-BTC/SPE, Fe-BTC/SPE, and Fe-BTC@Cu-BTC/SPE, compared to bare SPE (0.0003). From these obtained results, it can be concluded that the modification with MOF materials led to the impressive enhancements in terms of electron transfer, the electrochemical active area ( $A$ ), and the electron transfer reaction kinetics at the electrode/electrolyte interface. Particularly, benefiting from the smallest peak separation and the lowest charge transfer resistance  $R_{ct}$ , and the largest  $A$  as well as  $k_{et}$  values, Fe-BTC@Cu-BTC/SPE exhibited the highest current intensity, promising the expected enhancement of sensing performance in the next section.

### 3.3. Electrochemical behaviors of $\text{Pb}^{2+}$ on the proposed electrodes

As a first step in evaluating the sensing performance of the proposed electrode, the electrochemical behavior of  $\text{Pb}^{2+}$  was investigated using CV and DPASV measurements. CV curves were recorded at a scan rate of 50  $\text{mV s}^{-1}$  in 0.1 M AcB buffer solution (pH 4), both in the absence and presence of 10 ppm  $\text{Pb}^{2+}$  (Fig. 5a). In the presence of  $\text{Pb}^{2+}$ , a pair of well-defined redox peaks was observed at around  $-0.71$  V (oxidation peak) and  $-0.81$  V (reduction peak), consistent with the known redox behavior of  $\text{Pb}^{2+}$ . In contrast, no distinct redox peaks were detected in the absence of  $\text{Pb}^{2+}$ , aside from a minor reduction peak attributed to hydroxyl groups on the electrode surface. More importantly, the oxidation current signal at  $-0.71$  V

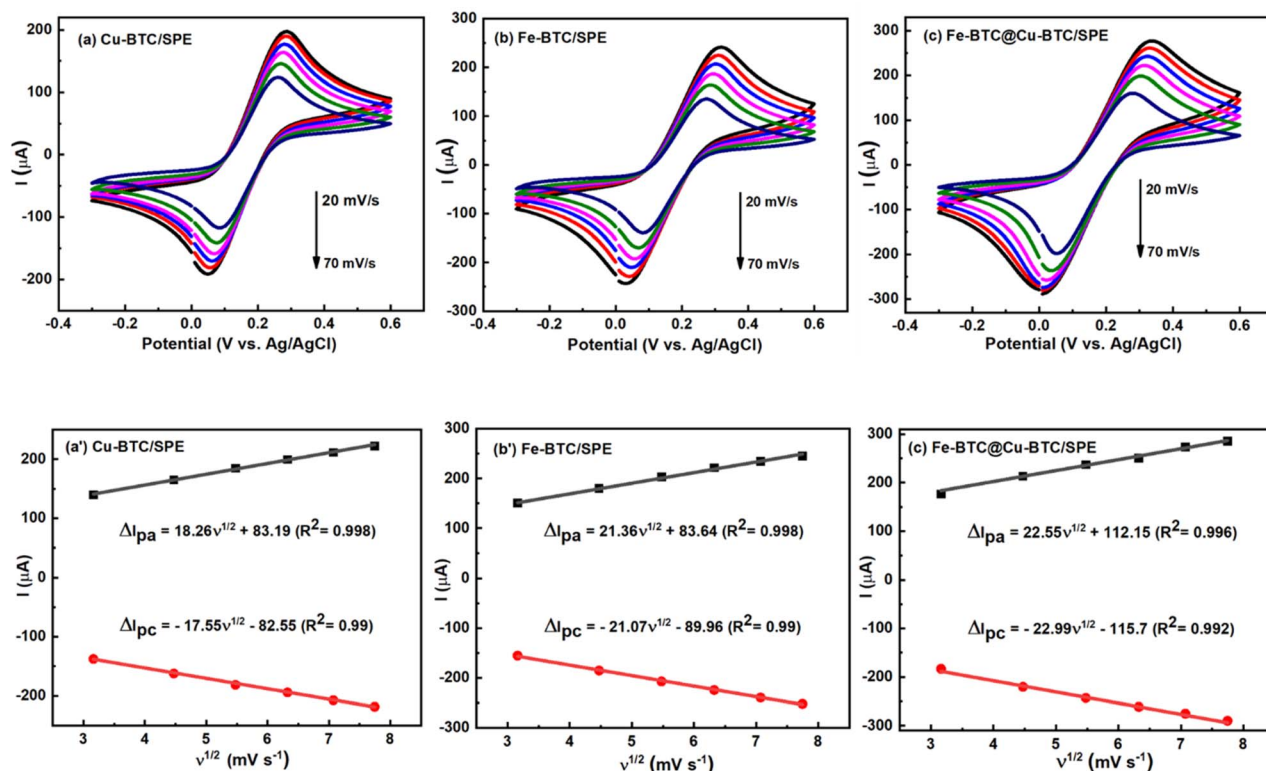


Fig. 4 (a–c) CV profiles of modified electrodes at various scan rates (20–70  $\text{mV s}^{-1}$ ) in 0.1 M KCl containing 5 mM  $[\text{Fe}(\text{CN})_6]^{3-/4-}$ ; and (a'–c') the corresponding linear plots of reduction peak current response ( $I_p$ - $\mu\text{A}$ ) and sqrt. of scan rate ( $\nu^{1/2}$ ).



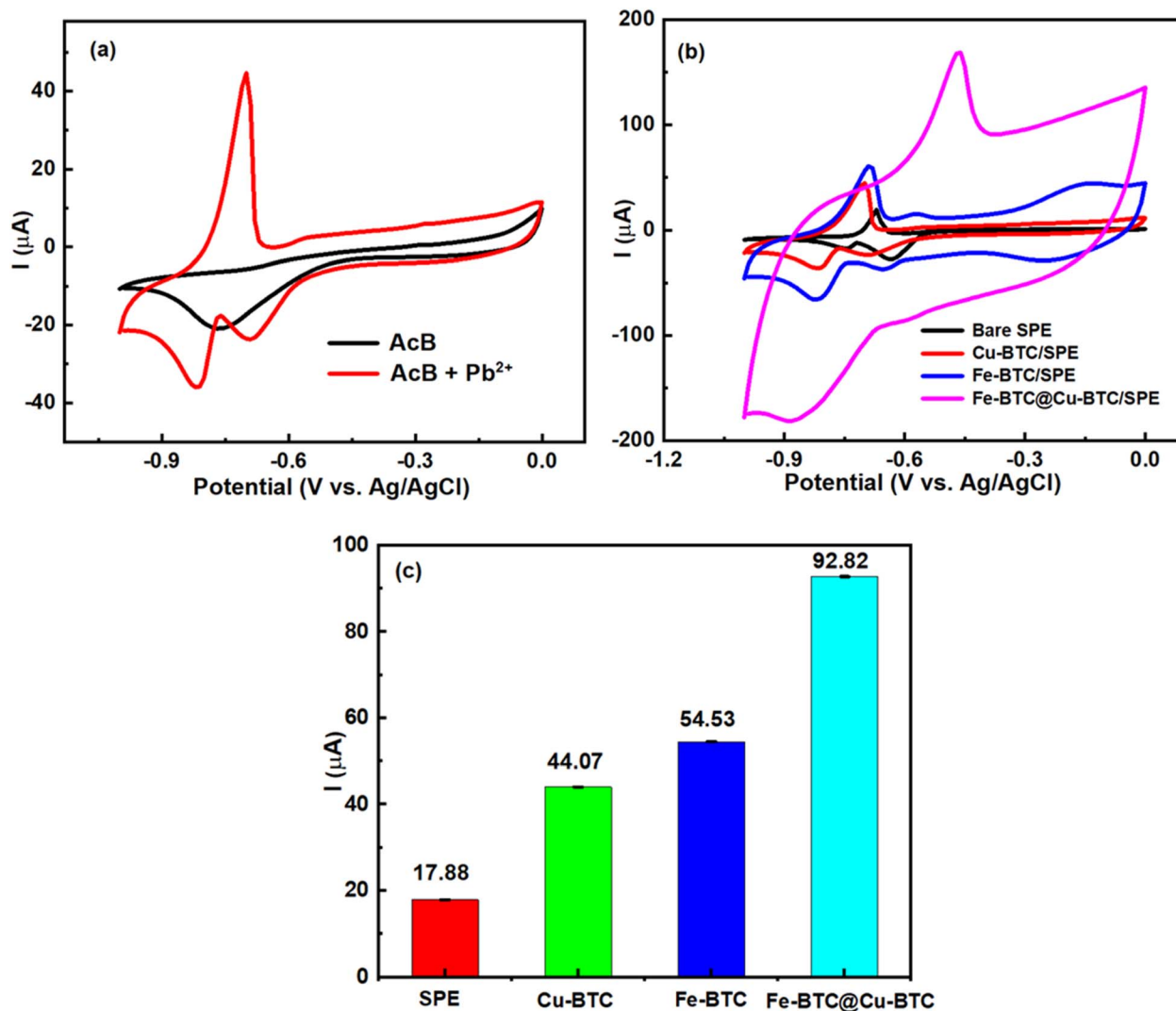


Fig. 5 (a) CV curves recorded in 0.1 M AcB buffer solution (pH 4) with the absence and presence of 10 ppm Pb<sup>2+</sup>; (b) CV curves of bare SPE and modified electrodes in 0.1 M AcB buffer solution (pH 4) containing 10 ppm Pb<sup>2+</sup>; (c) the plot of comparing oxidation peak currents between bare SPE and modified electrodes, respectively.

exhibited a higher and more sensitive current response compared to the corresponding reduction peak at  $-0.81$  V, and was therefore selected as the quantitative signal for Pb<sup>2+</sup> detection. To further assess electrode performance, the oxidation peak currents were compared across different electrode configurations, as shown in Fig. 5b. The Fe-BTC@Cu-BTC/SPE demonstrated the highest current intensity, which was approximately 1.7 and 2.1 times greater than those of Fe-BTC/SPE and Cu-BTC/SPE, respectively, and nearly 5 times higher than that of the bare SPE. Additionally, in-depth observation can conclude that the trend of peak potential shift was also observed when the anodic peak rose at a lower potential around  $-0.47$  V for the Fe-BTC@Cu-BTC/SPE, meanwhile, that at  $-0.71$  V for the bare SPE, indicating improved electron transfer kinetics. These results suggest that the Fe-BTC@Cu-BTC composite significantly enhances the electrochemical activity of Pb<sup>2+</sup> at the electrode/electrolyte interface, confirming its suitability as a high-performance platform for Pb<sup>2+</sup> sensing.

These findings are further supported by electrochemical studies conducted in 0.1 M KCl containing 5.0 mM Fe<sup>2+</sup>/Fe<sup>3+</sup> redox probe molecules.

To further study on the electrochemical behaviors as well as kinetics of the modified electrodes toward Pb<sup>2+</sup> detection, CV technique was used under the scan rate ranging from 20 to 70 mV s<sup>-1</sup> in 0.1 M AcB buffer (pH 4) solution containing 10 ppm Pb<sup>2+</sup>. For all modified electrodes, as the scan rate increased, the oxidation peak current increased gradually (Fig. 6). Notably, there was a good linear relationship between peak current ( $I$ -μA) and scan rate ( $\nu$ -mV s<sup>-1</sup>), implying the targeted Pb<sup>2+</sup> ions exist and transfer process in an adsorption state at the electrode/electrolyte interface. The regression equation was obtained as follows:

$$I_p (\mu\text{A}) = 0.436\nu (\text{mV s}^{-1}) + 20.61 (R^2 = 0.995) \text{ at Cu-BTC/SPE}$$

$$I_p (\mu\text{A}) = 0.568\nu (\text{mV s}^{-1}) + 22.73 (R^2 = 0.993) \text{ at Fe-BTC/SPE}$$



$$I_p (\mu\text{A}) = 1.205\nu (\text{mV s}^{-1}) + 34.55 (R^2 = 0.998) \text{ at Fe-BTC@Cu-BTC/SPE}$$

According to that, the adsorption capacity ( $I$ ) of the electroactive sites of the modified electrode surface can be determined from the slope value of the equation between  $I_p$  vs. scan rate by using the Brown-Anson model, which was based on the following equation:<sup>31–35</sup>  $I_p = n^2 F^2 \nu A \Gamma / 4RT$ , where  $n$  is the total number of electrons transferred ( $n = 2$ ) in the electrode reaction,  $F$  is the Faraday constant ( $96485 \text{ C mol}^{-1}$ ),  $I$  is adsorption capacity ( $\text{mol cm}^{-2}$ ),  $A$  is the surface area of the electrode,  $\nu$  is the scan rate,  $R$  is the gas constant ( $8.314 \text{ J mol}^{-1} \text{ K}^{-1}$ ), and  $T$  is the absolute temperature ( $298 \text{ K}$ ). The adsorption capacity ( $I$ ) of  $\text{Pb}^{2+}$  at Fe-BTC@Cu-BTC/SPE was equal to about  $1.48 \times 10^{-9} \text{ mol cm}^{-2}$ , which was considerably higher than that of Cu-BTC/SPE and Fe-BTC/SPE ( $8.92 \times 10^{-10}$  and  $9.29 \times 10^{-10} \text{ mol cm}^{-2}$ ). Furthermore, it was observed that there were slight shifts of reduction peak potential towards more negative values at higher scan rates, which was explained due to the formation of a diffusion layer on the electrode surface, causing the transfer limitation of charge and electrons. Particularly, the correlation between the anodic peak potentials ( $E_{\text{pa}}$ ) and  $\ln(\nu)$  was determined in good linear relationships of  $E_{\text{pa}} (\text{V}) = -0.0209 \ln(\nu) (\text{mV s}^{-1}) - 0.628 (R^2 = 0.99)$  for Cu-BTC/SPE and  $E_{\text{pa}} (\text{V}) = -0.0233 \ln(\nu) (\text{mV s}^{-1}) - 0.6 (R^2 = 0.99)$  for Fe-BTC/SPE, and  $E_{\text{pa}} (\text{V}) = -0.0503 \ln(\nu) (\text{mV s}^{-1}) - 0.29 (R^2 = 0.99)$ , respectively (Fig. S2). Based on the Laviron theory, the linear relationship between  $E_p$  and  $\ln(\nu)$  in an adsorption-controlled irreversible process can be estimated by the following equation:<sup>31,33,34</sup>

$$E_p = E_0 + (RT/\alpha nF) \times \ln(RT k_0 / \alpha nF) - (RT/\alpha nF) \times \ln(\nu)$$

Following this, the charge transfer coefficient value ( $\alpha$ ) of Fe-BTC, Cu-BTC, and Fe-BTC@Cu-BTC/SPE was determined from the slope value, corresponding to  $RT/\alpha nF$ . Herein, the total number of electrons transferred ( $n$ ) in the electrochemical stripping of  $\text{Pb}^0$  atoms and  $\text{Pb}^{2+}$  ions reduction was equal to 2. By this, the calculated values of  $\alpha$  were near 0.407, 0.454, and 0.979 for Cu-BTC, Fe-BTC, and Fe-BTC@Cu-BTC/SPE, respectively.

The above-discussed analysis and the obtained result prove that the effective integration of Fe-BTC and Cu-BTC MOF materials significantly enhanced the electrochemical characteristics and sensing performance towards  $\text{Pb}^{2+}$  detection compared to their individual counterparts. To explain this, first of all, the dual application of microwave and electrochemical processes not only helped create a high-purity ion-rich solution, but also provided a fast and uniform heating process. These conditions promoted the formation of homogeneous MOF structures with distinct morphological features. Beyond synthesis, the composite's geometric configuration played a crucial role. The good distribution of Fe-BTC particles on the plate-like Cu-BTC surface, as described SEM images, demonstrated the outstanding efficiency in preventing the agglomeration of the poor-defined shape Fe-BTC particles and in

decreasing the material's size. The strong compatibility between Fe-BTC and Cu-BTC resulted in a stable, open three-dimensional framework. This 3D-geometric assembly of the composite remarkably contributed to an increase in in-depth surface area and accessibility of electroactive sites, improved the conductivity and functionality of surface material active responsive local sites, as well as promoted the transfer of the electrolyte ions. Notably, the point-to-face exposure of these two MOF structures is also considered to be essential for the rich in the transfer of electron conduction and supports the rapid charge mobility.

The insight electrochemical activity and the high capacity of targeted  $\text{Pb}^{2+}$  ions adsorption were also deeply understood through structural and compositional analysis of the as-prepared electrodes. According to that, the large difference in the calculated adsorption capacity ( $I$ ) values provided compelling evidence of the difference in adsorption ability between modifying materials used. Returning to the material characteristics of Fe-BTC and Cu-BTC, they are known for their porous frameworks and abundance of electrochemically active sites, arising from the partially naked metal centers (Cu and Fe) with unsaturated coordination environments. These open unsaturated metal centers are critical for interacting with target analytes such as  $\text{Pb}^{2+}$  ions. More importantly, when comparing the adsorption capacity ( $I$ ) value between Cu-BTC/SPE and Fe-BTC/SPE, the adsorption capacities were relatively close  $8.92 \times 10^{-10}$  and  $9.29 \times 10^{-10} \text{ mol cm}^{-2}$ , respectively. This behaviour was ascribed to the higher polarizing power of  $\text{Fe}^{3+}$  ( $[\text{Ar}] 3 \text{ d}^5$ ) in comparison to  $\text{Cu}^{2+}$  ( $[\text{Ar}] 3 \text{ d}^9$ ), due to its higher charge, as supported by prior studies.<sup>9,21</sup> Remarkably, the Fe-BTC@Cu-BTC/SPE exhibited a 1.6-fold increase in adsorption capacity relative to the individual MOFs. This enhancement is credited to the coexistence of both Cu and Fe metal centers within the composite's pore surfaces, as well as its 3D-open framework with ordered transport channels, higher surface area, and greater pore uniformity. These features collectively facilitated more efficient  $\text{Pb}^{2+}$  ions adsorption and improved overall sensing performance. As a result, Fe-BTC@Cu-BTC/SPE exhibits a suite of favorable characteristics that position it as a promising candidate for sensing applications. These include enhanced surface area and pore volume, improved electronic conductivity and charge transport efficiency, elevated adsorption capacity, superior ion diffusion dynamics, and robust interaction capability with  $\text{Pb}^{2+}$  ions. Collectively, these attributes contribute to its high-performance potential in electrochemical detection systems.

The investigation of the optimized electrochemical response of the proposed electrode in terms of pH and equilibrium time values is considered as one of the most crucial steps in elucidating the electrochemical behavior at the electrode/electrolyte interface and establishing ideal conditions for  $\text{Pb}^{2+}$  detection. According to that, a series of experiments was conducted on Fe-BTC@Cu-BTC/SPE against different pHs from 3 to 8 and varying equilibrium times from 30 to 150 s. Differential pulse anodic stripping voltammetry (DPASV) measurements were used to evaluate the current intensity ( $I_p$ ) as a function of pH and equilibrium time, as illustrated in Fig. 7a and b. The anodic peak intensity of  $\text{Pb}^{2+}$  reached its maximum at pH 4, followed by a gradual decline as pH increased from 4 to 8. This behavior is



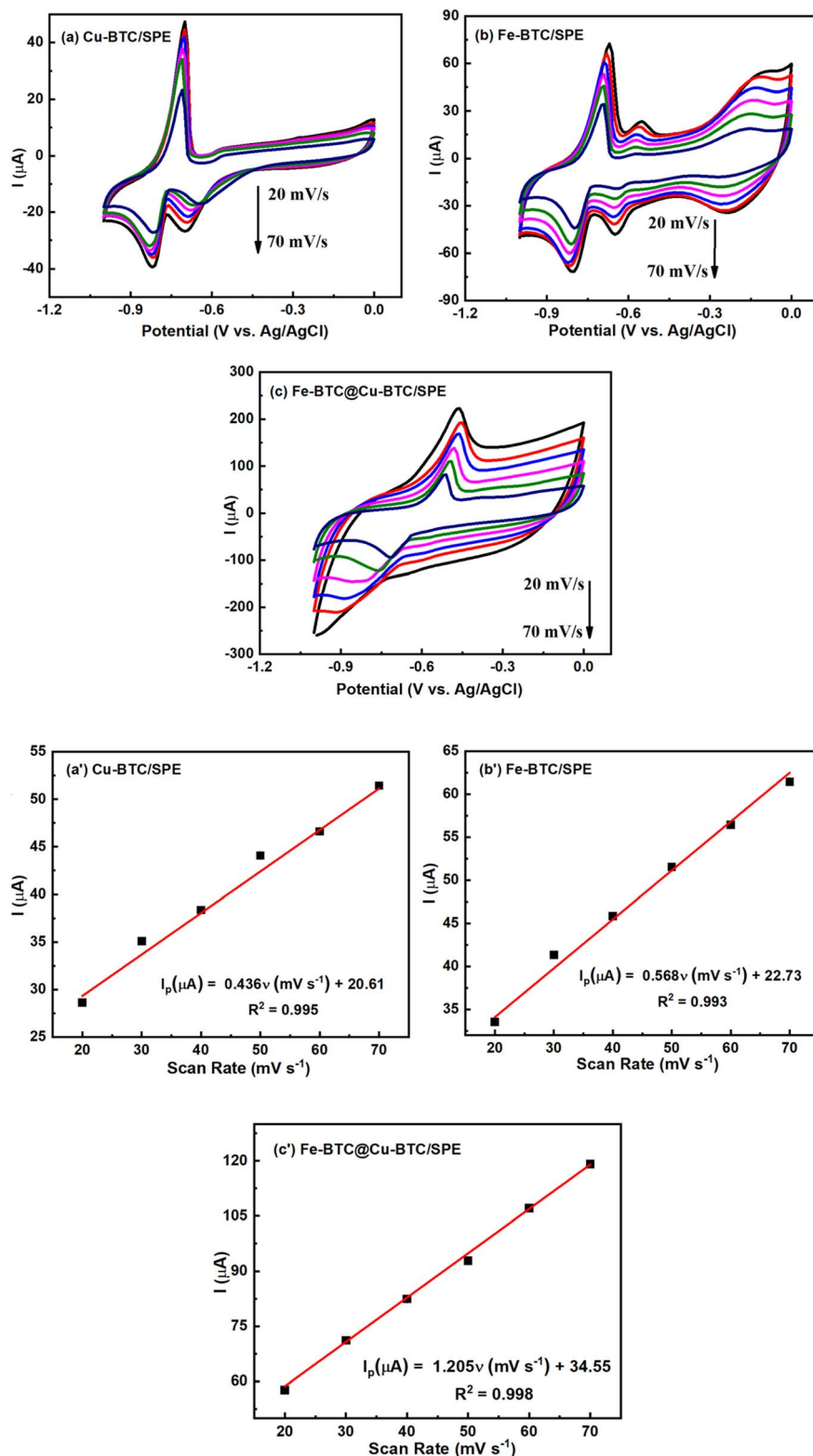


Fig. 6 (a–c) CVs responses of 10 ppm  $\text{Pb}^{2+}$  at the modified SPE in 0.1 M AcB buffer (pH 4) solution at different scan rates, corresponding to the calibration plots (a'–c').

explained due to the protonation of amino groups ( $-\text{NH}_2$ ) on MOF under very strongly acidic solutions, as well as the hydrolytic instability of  $\text{Pb}^{2+}$  in less acidic environments.

Similarly, the oxidation peak current of  $\text{Pb}^{2+}$  increased continuously with increasing equilibrium time until the current intensity attained the highest value at 90 s before declining.



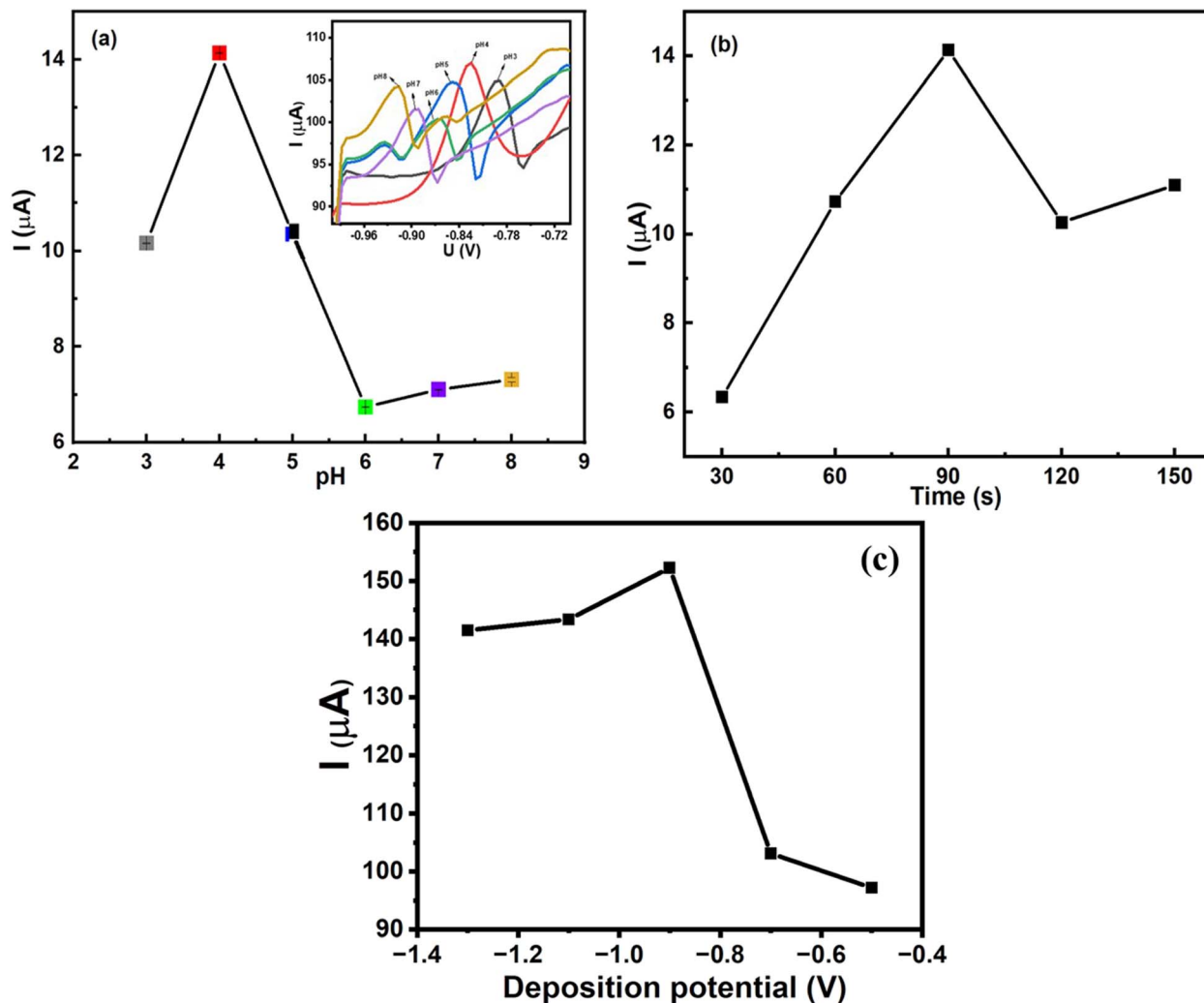


Fig. 7 (a) and (b) The plots of peak currents ( $I_p$ ) vs. pH and  $T_{equilibrium}$  values from DPASV measurements at Fe-BTC@Cu-BTC/SPE in 0.1 M AcB solution (pH 4) containing 1 ppm  $Pb^{2+}$  (inset: DPASV curves with different pH). Scan rate of 15  $mV s^{-1}$ ; (c) the plots of peak current ( $I_p$ ) vs. various deposition potentials in 0.1 M AcB buffer solution (pH 4) containing 10 ppm  $Pb^{2+}$ .

This trend may be explained by considering that the absorption of  $Pb^{2+}$  by  $-NH_2$  onto the MOF materials reached a saturation point at high  $Pb^{2+}$  concentrations. Based on the obtained results, it is noted that pH 4 and an equilibrium time of 90 s were chosen to be appropriate parameters for the electrochemical oxidation reaction process of  $Pb^{2+}$ . Besides, the effect of deposition potential was investigated by recording current response from DPASV measurements at various deposition potential values, as shown in Fig. 7c. The oxidation of  $Pb^{2+}$  was highly dependent on the time for pretreating the electrode surface since the adsorption controlled the oxidation of  $Pb^{2+}$ . In Fig. 7c, the peak intensity initially increased and then decreased, achieving a maximum value at an electric potential of  $-0.9$  V. Consequently,  $-0.9$  V was identified as the optimal deposition potential and was employed in subsequent experiments.

Under the above-optimized experimental conditions, the electrochemical sensing performance of the proposed electrode for  $Pb^{2+}$  detection was evaluated using DPASV measurements. The sensing mechanism involves main steps: pre-enrichment

and stripping, which can be described by the fundamental reaction:  $Pb^{2+} + 2e^- \leftrightarrow Pb^0$

Step 1: Pre-enrichment (Reduction reaction)

$Pb^{2+}$  ions are attracted and strongly adsorbed onto the  $Fe^{3+}$  and  $Cu^{2+}$  coordinatively unsaturated sites of the Fe-BTC@Cu-BTC-modified electrode. These adsorbed  $Pb^{2+}$  ions accept electrons at the electrode surface and are reduced to metallic  $Pb^0$ , accumulating on the modified electrode.

Step two: Stripping (Oxidation reaction)

Upon applying a reverse (anodic) potential, the pre-enriched  $Pb^0$  is re-oxidized to  $Pb^{2+}$  and released back into the electrolyte. The electrons generated during this oxidation process return to the electrode, producing a characteristic stripping peak current, which is used for quantitative detection.

Step three:

The redox couples within the Fe-BTC@Cu-BTC serve as electron-transfer mediators, facilitating charge exchange between the electrode and  $Pb^{2+}/Pb^0$ . This redox cycling enhances the kinetics of the  $Pb^{2+}$  redox reactions, lowers



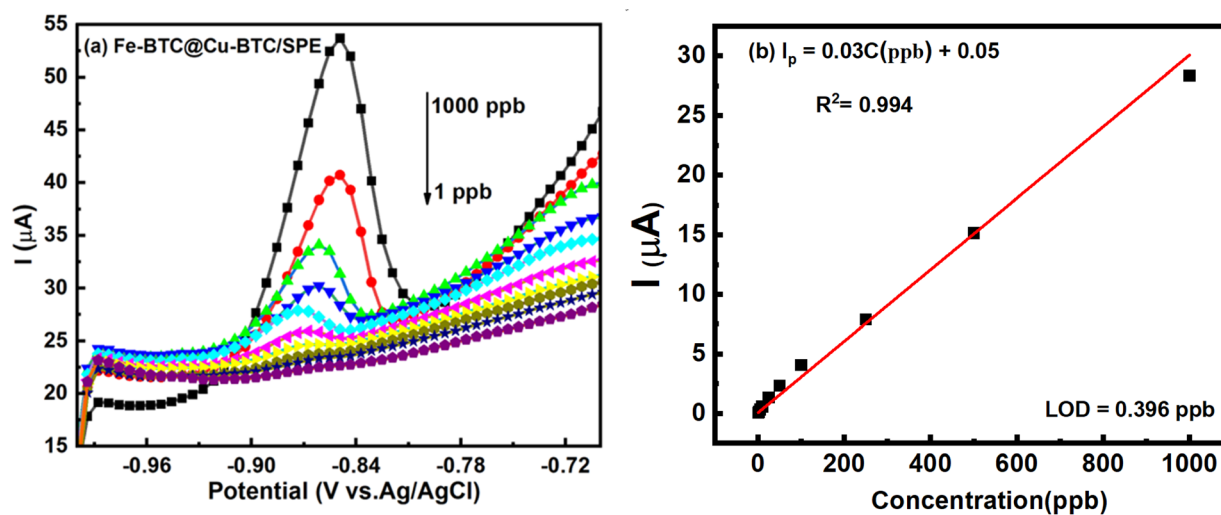


Fig. 8 (a) DPASV curves recorded at Fe-BTC@Cu-BTC/SPE for various  $\text{Pb}^{2+}$  concentrations in 0.1 M AcB buffer (pH 4) solution; corresponding to (b) the calibration plots of peak current intensity vs. various  $\text{Pb}^{2+}$  concentrations.

charge-transfer resistance, and ultimately amplifies the stripping current. As a result, the Fe-BTC@Cu-BTC/SPE sensor exhibited improved sensitivity and detection performance toward  $\text{Pb}^{2+}$ .

From the perspective of an electronic structure, in this work, the presence of coordinatively unsaturated metal sites ( $\text{Cu}^{2+}$  and  $\text{Fe}^{3+}$ ) in Fe-BTC@Cu-BTC composite plays a central role in the redox process due to their strong interactions with  $\text{Pb}^{2+}$ . In this heterostructure, the  $\text{Fe}^{3+}$  centers act as strong Lewis-acidic adsorption sites, while the  $\text{Cu}^{2+}$  centers enhance electron transfer and mobility. This combination creates more energetically favorable  $\text{Pb}^{2+}$  adsorption compared with either Fe-BTC or Cu-BTC alone. Furthermore, the synergistic electronic interaction between the two frameworks induces interfacial charge redistribution, which provides faster charge-transfer pathways and more effective binding sites when  $\text{Pb}^{2+}$  interacts with the composite surface. The coexistence of Fe and Cu clusters also opens multiple electron-transfer pathways, reducing the overall charge-transfer resistance. In addition, the 3D open-framework architecture with shorter and more ordered electron-transport pathways, larger surface area, abundant exposed metal sites, and improved pore uniformity remarkably reduces charge-transfer resistance. These structural advantages also enhance electron exchange at the active adsorption sites and facilitate the pre-enrichment of  $\text{Pb}^{2+}$ , ultimately improving the electrochemical detection performance of the composite.

According to that, the relationship between oxidation peak intensity measured by DPASV at a scan rate of  $6 \text{ mV s}^{-1}$  and  $\text{Pb}^{2+}$  concentration, was investigated. As illustrated in Fig. 8, the peak intensity increased proportionally with rising  $\text{Pb}^{2+}$  concentration and there is a good linear relationship between the peak current intensity and different  $\text{Pb}^{2+}$  concentrations starting from 1 ppb to 1000 ppb (Fig. 8b). For the lower  $\text{Pb}^{2+}$  concentration range, the linear regression equation was determined to be  $I_p (\mu\text{A}) = 0.03C (\mu\text{M}) + 0.05$  with a correlation coefficient of 0.994, indicating excellent linearity. The limits of

detection (LOD) and quantitation (LOQ) for  $\text{Pb}^{2+}$  were calculated based on signal-to-noise ratios of 3 and 10, yielding values of 0.396 ppb and 1.32 ppb, respectively. To benchmark the analytical performance of the Fe-BTC@Cu-BTC/SPE sensor, a comparative analysis was conducted against previously reported electrodes modified with various MOF-based materials, including those incorporating precious metals. As summarized in Table 1, the proposed sensor demonstrated superior performance in both linear detection range and LOD. Notably, it achieved these results using low-cost materials and a simple, scalable synthesis method. These findings highlight the Fe-BTC@Cu-BTC/SPE sensor as a highly sensitive, selective, and economically viable platform for trace heavy metal analysis, with strong potential for practical deployment in environmental and consumer product monitoring.

For practical applications, the repeatability and selectivity are critical parameters for evaluating the reliability of the proposed Fe-BTC@Cu-BTC/SPE sensor. In which, the repeatability was evaluated by conducting ten consecutive DPASV measurements under identical experimental conditions. The relative standard deviation of the peak intensity was calculated to be 1.141%, indicating excellent repeatability. Furthermore, to test the selectivity, the current response of Fe-BTC@Cu-BTC/SPE toward  $\text{Pb}^{2+}$

Table 1 Comparison of Fe-BTC@Cu-BTC/SPE performance with other modified electrodes reported for  $\text{Pb}^{2+}$  detection

Modified electrodes	Linear range ( $\mu\text{M}$ )	LOD (M)	Ref.
Cu-MOF/GCE	0.01–1	$4.9 \times 10^{-9}$	36
Au NPs@Cu-BTC	0.01–1000	$1 \times 10^{-9}$	15
MIL-100(Cr)/GCE	0–10	$4.8 \times 10^{-8}$	37
$\text{NH}_2$ -MIL-53(Cr)/GCE	0.4–80	$3.05 \times 10^{-8}$	38
$\text{NH}_2$ -MIL-88(Fe)-rGO/GCE	0.01–0.3	$1 \times 10^{-8}$	39
Ni-MOF/GCE	0.5–6	$5.08 \times 10^{-7}$	40
Fe-BTC@Cu-BTC/SPE	0.005–4.83	$1.9 \times 10^{-9}$	This work



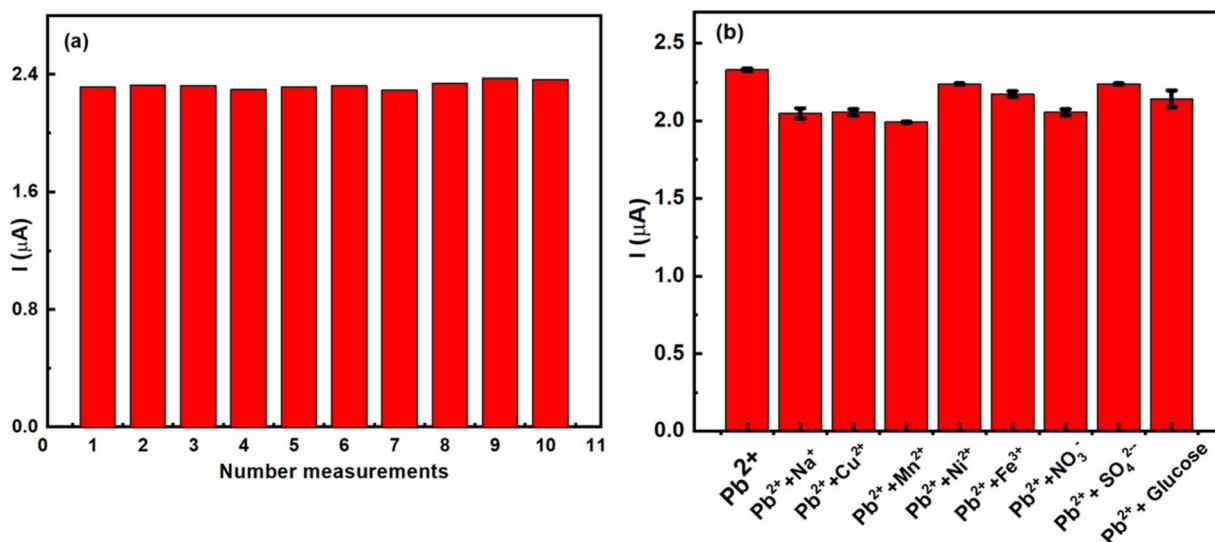


Fig. 9 (a) The repeatability and (b) anti-interfering ability of Fe-BTC@Cu-BTC/SPE toward  $\text{Pb}^{2+}$  detection in 0.1 M AcB buffer (pH 4) solution containing 50 ppb  $\text{Pb}^{2+}$  by DPASV measurements.

Table 2 Determination results of  $\text{Pb}^{2+}$  in spiked shampoo samples using DPASV measurements ( $n = 4$ )

Electrode	Amount spiked (ppb)	Amount found (ppb)	Recovery (%)	RSD (%)
Fe-BTC@Cu-BTC/SPE	75	70.69	94.25	1.00
	25	23.59	94.36	1.10
	10	9.36	93.56	1.06
	5	4.56	91.11	1.35

detection in the presence of various potential interferents, including  $\text{Na}^+$ ,  $\text{Cu}^{2+}$ ,  $\text{Mn}^{2+}$ ,  $\text{Ni}^{2+}$ ,  $\text{Fe}^{3+}$ ,  $\text{NO}_3^-$ ,  $\text{SO}_4^{2-}$ , and glucose was recorded. As exhibited in Fig. 9b, the  $\text{Pb}^{2+}$  oxidation peak current remained largely unaffected, even when these interferents were present at high concentrations. The percentage recoveries for  $\text{Pb}^{2+}$  detection exceeded 86% across most tested species, confirming the sensor's strong anti-interference capability and high selectivity in complex sample matrices.

To further evaluate the practical applicability of the proposed Fe-BTC@Cu-BTC/SPE sensor,  $\text{Pb}^{2+}$  concentration in a commercial shampoo sample was determined using the standard addition method. The shampoo sample served as a blank matrix, and known quantities of  $\text{Pb}^{2+}$  standard solution was added to prepare spiked samples. As summarized in Table 2, the sensor successfully detected  $\text{Pb}^{2+}$  at ppb levels. The recovery rates for the spiked samples ranged from 91.11% to 94.36%, while the RSDs were between 1.00% and 1.35%. These results underscore the sensor's potential for environmental and consumer product monitoring, offering a reliable, sensitive, and cost-effective platform for trace  $\text{Pb}^{2+}$  detection in complex systems.

## 4. Conclusions

In this study, Cu-BTC, Fe-BTC, and Fe-BTC@Cu-BTC composites were successfully synthesized *via* a microwave-assisted

electrochemical method in the presence of  $\text{NaCl}/\text{H}_2\text{O}$  and  $\text{H}_3\text{BTC}$  solutions. After microwave irradiation, the formation of particle-shaped Fe-BTC and plate-shaped Cu-BTC was observed. Notably, the Fe-BTC@Cu-BTC composite was obtained with Cu-BTC plates serving as an effective substrate for the uniform distribution of Fe-BTC particles. This spatial arrangement is likely driven by hydrogen bonding interactions between functional groups inherent to the MOF frameworks. The new electrochemical sensors for the detection of trace  $\text{Pb}^{2+}$  were developed using the proposed MOFs-modified SPEs. All three modified electrodes exhibited good electrochemical characteristics and high responses for  $\text{Pb}^{2+}$  compared to the bare SPE. Among them, Fe-BTC@Cu-BTC/SPE could be considered as a promising electroanalytical sensory platform owing to the synergistic effects arising from the synergistic integration of Fe-BTC particles and Cu-BTC plates, such as the good electric conductivity, high electrochemical active surface area, and impressive transfer kinetics. As a result, the Fe-BTC@Cu-BTC/SPE sensor exhibited a low overpotential for  $\text{Pb}^{2+}$  oxidation, a broad linear detection range, low LOD, high sensitivity, great selectivity, and high possibility for practical applicability in shampoo sample analysis. Specifically, the sensor achieved a linear detection range from 1 and 1000 ppb  $\text{Pb}^{2+}$ , and the LOD as low as 0.396 ppb ( $S/N = 3$ ). In real sample analysis, the sensor demonstrated high recovery rates ranging from 91.11 to



94.36%, confirming its practical applicability for Pb<sup>2+</sup> detection in shampoo matrices. Owing to its excellent analytical sensitivity, straightforward fabrication, and cost-effective design, the Fe-BTC@Cu-BTC/SPE sensor presents significant potential for monitoring Pb<sup>2+</sup> contamination in consumer products. Furthermore, this work introduces a rapid and scalable strategy for synthesizing MOF materials with tailored microstructures and provides valuable insights into the structural and compositional factors that govern their electrochemical behavior and sensing capabilities.

## Author contributions

T. N. Pham: methodology, formal analysis, investigation, writing – original draft; N. L. N. Trang: validation, investigation; O. V. Hoang: validation, investigation, formal analysis; T. V. Manh: methodology, validation; N. Q. Hoa: methodology, validation; V. D. Lam: formal analysis, writing – review & editing; P. M. Huong: methodology, writing – review & editing; Anh-Tuan Le: conceptualization, methodology, supervision, writing – review & editing, project administration.

## Conflicts of interest

The authors declare that they have no known competing financial interests or personal relationships that could have appeared to influence the work reported in this paper.

## Data availability

The data supporting this article have been included as part of the figures and Table, as well as the supplementary information (SI). Supplementary information is available. See DOI: <https://doi.org/10.1039/d5ra08888g>.

## Acknowledgements

This research was supported by the Phenikaa University, Vietnam under grant number (PU2023–1-A-20). The authors would like to acknowledge the support for electrochemical measurements from NEB Lab (Phenikaa University), SEM & XRD measurements from IOP-VAST & HUS-VNU, Hanoi.

## References

- 1 L. Ji, Q. Cheng, K. Wu and X. Yang, Cu-BTC frameworks-based electrochemical sensing platform for rapid and simple determination of Sunset yellow and Tartrazine, *Sens. Actuators, B*, 2016, **231**, 12–17.
- 2 S. Jyotsna Sahoo, B. Barik, B. Maji, P. S. Nayak, N. Behera and P. Dash, A redox accessible Cu-BTC metal organic framework-based nanocomposite for selective and sensitive electrochemical sensing of Triclosan in real sample, *J. Electroanal. Chem.*, 2023, **943**, 117589.
- 3 C. Li and K. Wu, Cu-BTC frameworks based electrochemical sensor for hazardous malachite green in aquaculture, *Anal. Chim. Acta*, 2021, **1162**, 338473.
- 4 S. L. James, Metal–organic frameworks, *Chem. Soc. Rev.*, 2003, **32**, 276–288.
- 5 Y.-K. Seo, G. Hundal, I. T. Jang, Y. K. Hwang, C.-H. Jun and J.-S. Chang, Microwave synthesis of hybrid inorganic–organic materials including porous Cu<sub>3</sub>(BTC)<sub>2</sub> from Cu(II)-trimesate mixture, *Microporous Mesoporous Mater.*, 2009, **119**, 331–337.
- 6 Y. Cao, L. Wang, C. Shen, C. Wang, X. Hu and G. Wang, An electrochemical sensor on the hierarchically porous Cu-BTC MOF platform for glyphosate determination, *Sens. Actuators, B*, 2019, **283**, 487–494.
- 7 L. Ji, L. Peng, T. Chen, X. Li, X. Zhu and P. Hu, Facile synthesis of Fe-BTC and electrochemical enhancement effect for sunset yellow determination, *Talanta Open*, 2022, **5**, 100084.
- 8 M. C. Maridevaru, A. Dube, R. Kaimal, A. A. Souwaileh, S. Kannadasan and S. Anandan, An iron metal–organic framework-based electrochemical sensor for identification of Bisphenol-A in groundwater samples, *Anal.*, 2024, **149**, 3325–3334.
- 9 G. Autié-Castro, E. Reguera, C. L. Cavalcante, A. S. Araujo and E. Rodríguez-Castellón, Surface acid-base properties of Cu-BTC and Fe-BTC MOFs. An inverse gas chromatography and n-butylamine thermo desorption study, *Inorg. Chim. Acta*, 2020, **507**, 119590.
- 10 V. M. V and G. Nageswaran, Review-Direct Electrochemical Synthesis of Metal Organic Frameworks, *J. Electrochem. Soc.*, 2020, **167**, 155527.
- 11 N. Zalpour, M. Roushani and H. Hosseini, Polydopamine imprinted polymer-based tunable electrochemical synthesis of copper benzene-1, 3, 5-tricarboxylate metal-organic framework film as a hybrid dual recognition element for ultra-trace sensing of pregabalin (lyrica), *Sens. Actuators, B*, 2022, **370**, 132418.
- 12 Y. Chen, D. Ni, X. Yang, C. Liu, J. Yin and K. Cai, Microwave-assisted synthesis of honeycomblike hierarchical spherical Zn-doped Ni-MOF as a high-performance battery-type supercapacitor electrode material, *Electrochim. Acta*, 2018, **278**, 114–123.
- 13 T. Qi, Z. Yuan and F. Meng, Highly sensitive and highly selective lead ion electrochemical sensor based on zn/cu-btc-nh2 bimetallic MOFs with nano-reticulated reinforcing microstructure, *Anal. Chim. Acta*, 2024, **1318**, 342896.
- 14 C. Li, J. Hao and K. Wu, Triethylamine-controlled Cu-BTC frameworks for electrochemical sensing fish freshness, *Anal. Chim. Acta*, 2019, **1085**, 68–74.
- 15 G. A. Bodkhe, B. S. Hedau, M. A. Deshmukh, H. K. Patil, S. M. Shirsat, D. M. Phase, K. K. Pandey and M. D. Shirsat, Detection of Pb(II): Au Nanoparticle Incorporated CuBTC MOFs, *Front Chem.*, 2020, **8**, 803.
- 16 J. Zhou, X. Li, L. Yang, S. Yan, M. Wang, D. Cheng, Q. Chen, Y. Dong, P. Liu, W. Cai and C. Zhang, The Cu-MOF-199/single-walled carbon nanotubes modified electrode for simultaneous determination of hydroquinone and catechol with extended linear ranges and lower detection limits, *Anal. Chim. Acta*, 2015, **899**, 57–65.



- 17 N. A. Travlou, K. Singh, E. Rodríguez-Castellón and T. J. Bandoz, Cu-BTC MOF-graphene-based hybrid materials as low concentration ammonia sensors, *J. Mater. Chem. A*, 2015, **3**, 11417–11429.
- 18 Y. Deng, S. Li, X. Ma, Y. Wu, C. Pang, M. Wang, J. Li and X. Zhi, Electrochemical chiral sensor for levofloxacin detection base on Cu/Fe-BTC amplification, *Microchim. Acta*, 2023, **190**, 435.
- 19 W. Y. Siew, N. H. H. Abu Bakar, M. Abu Bakar and A. Zainal Abidin, Influence of various Cu/Fe ratios on the surface properties of green synthesized Cu-Fe-BTC and it's relation to methylene blue adsorption, *J. Hazard. Mater.*, 2021, **416**, 125846.
- 20 W. Xiang, Y. Liao, J. Cui, Y. Fang, B. Jiao and X. Su, Room-temperature synthesis of Fe/Cu-BTC for effective removal of tetracycline antibiotic from aquatic environments, *Inorg. Chem. Commun.*, 2024, **167**, 112728.
- 21 N. Torres, J. Galicia, Y. Plasencia, A. Cano, F. Echevarría, L. F. Desdin-García and E. Reguera, Implications of structural differences between Cu-BTC and Fe-BTC on their hydrogen storage capacity, *Colloids Surf., A*, 2018, **549**, 138–146.
- 22 K. Lellala, Microwave-Assisted Facile Hydrothermal Synthesis of Fe<sub>3</sub>O<sub>4</sub>-GO Nanocomposites for the Efficient Bifunctional Electrocatalytic Activity of OER/ORR, *Energy Fuels*, 2021, **35**, 8263–8274.
- 23 R. Kumar, R. K. Singh, A. V. Alaferdov and S. A. Moshkalev, Rapid and controllable synthesis of Fe<sub>3</sub>O<sub>4</sub> octahedral nanocrystals embedded-reduced graphene oxide using microwave irradiation for high performance lithium-ion batteries, *Electrochim. Acta*, 2018, **281**, 78–87.
- 24 S. Li, J. Cui, X. Wu, X. Zhang, Q. Hu and X. Hou, Rapid in situ microwave synthesis of Fe<sub>3</sub>O<sub>4</sub>@MIL-100(Fe) for aqueous diclofenac sodium removal through integrated adsorption and photodegradation, *J. Hazard. Mater.*, 2019, **373**, 408–416.
- 25 Y. Wang, W. Cao, L. Wang, Q. Zhuang and Y. Ni, Electrochemical determination of 2,4,6-trinitrophenol using a hybrid film composed of a copper-based metal organic framework and electroreduced graphene oxide, *Microchim. Acta*, 2018, **185**, 315.
- 26 Z. Dong, Z. Mi, W. Shi, H. Jiang, Y. Zheng and K. Yang, High pressure effects on hydrate Cu-BTC investigated by vibrational spectroscopy and synchrotron X-ray diffraction, *RSC Adv.*, 2017, **7**, 55504–55512.
- 27 E. Rojas-García, D. C. García-Martínez, R. López-Medina, F. Rubio-Marcos, A. A. Castañeda-Ramírez and A. M. Maubert-Franco, Photocatalytic Degradation of Dyes Using Titania Nanoparticles Supported in Metal-Organic Materials Based on Iron, *Molecules*, 2022, **27**, 7078.
- 28 S. A. Siddiqui, A. Prado-Roller and H. Shiozawa, Room temperature synthesis of a luminescent crystalline Cu-BTC coordination polymer and metal-organic framework, *Mater. Adv.*, 2022, **3**, 224–231.
- 29 N. A. Khan, E. Haque and S. H. Jhung, Rapid syntheses of a metal-organic framework material Cu<sub>3</sub>(BTC)<sub>2</sub>(H<sub>2</sub>O)<sub>3</sub> under microwave: a quantitative analysis of accelerated syntheses, *Phys. Chem. Chem. Phys.*, 2010, **12**, 2625–2631.
- 30 N. N. Huyen, N. X. Dinh, H. Van Thanh, P. D. Thang and A.-T. Le, ZnCo<sub>2</sub>O<sub>4</sub> porous nanosheets-based sensing platform for ultra-sensitive detection of Pb(II) ion at sub-parts-per-trillion level in juice and beverage samples by using differential pulse anodic stripping voltammetry, *J. Food Compos. Anal.*, 2024, **134**, 106493.
- 31 T. N. Pham, D. N. Xuan, T. H. Van, V. L. Khanh, T. L. Minh, V. Q. Nguyen, D. L. Vu and A.-T. Le, Insight into the Influence of Analyte Molecular Structure Targeted on MoS<sub>2</sub>-GO-Coated Electrochemical Nanosensors, *Langmuir*, 2021, **37**, 12059–12070.
- 32 S. Bunnasit, K. Thamsirianunt, R. Rakthabut, K. Jeamjumnunja, C. Prasittichai and W. Siriwatcharapiboon, Sensitive Portable Electrochemical Sensors for Antibiotic Chloramphenicol by Tin/Reduced Graphene Oxide-Modified Screen-Printed Carbon Electrodes, *ACS Appl. Nano Mater.*, 2024, **7**, 267–278.
- 33 A. Paisanpisuttisin, P. Poonwattanapong, P. Rakthabut, P. Ariyasantichai, C. Prasittichai and W. Siriwatcharapiboon, Sensitive electrochemical sensor based on nickel/PDDA/reduced graphene oxide modified screen-printed carbon electrode for nitrite detection, *RSC Adv.*, 2022, **12**, 29491–29502.
- 34 V. H. Ong, T. N. Pham, V. M. Tien, N. X. Dinh, N. Thi Lan, N. Van Quy, T. N. Bach, V. D. Lam, L. M. Tung and A.-T. Le, Toward a comprehensive understanding of effect of cation distribution and M<sup>2+</sup> constituent in spinel ferrite nanocrystals MFe<sub>2</sub>O<sub>4</sub> (M = Co, Mn, and Ni) on the electrochemical response in sensitive detection of chloramphenicol, *J. Alloys Compd.*, 2023, **949**, 169880.
- 35 D. Pamuk, İ. H. Taşdemir, A. Ece, E. Canel and E. Kılıç, Redox Pathways of Aliskiren Based on Experimental and Computational Approach and Its Voltammetric Determination, *J. Braz. Chem. Soc.*, 2013, **24**, 1276–1286.
- 36 Y. Wang, Y. Wu, J. Xie and X. Hu, Metal-organic framework modified carbon paste electrode for lead sensor, *Sens. Actuators, B*, 2013, **177**, 1161–1166.
- 37 D. Wang, Y. Ke, D. Guo, H. Guo, J. Chen and W. Weng, Facile fabrication of cauliflower-like MIL-100(Cr) and its simultaneous determination of Cd<sup>2+</sup>, Pb<sup>2+</sup>, Cu<sup>2+</sup> and Hg<sup>2+</sup> from aqueous solution, *Sens. Actuators, B*, 2015, **216**, 504–510.
- 38 H. Guo, D. Wang, J. Chen, W. Weng, M. Huang and Z. Zheng, Simple fabrication of flake-like NH<sub>2</sub>-MIL-53(Cr) and its application as an electrochemical sensor for the detection of Pb<sup>2+</sup>, *Chem. Eng. J.*, 2016, **289**, 479–485.
- 39 S. Duan and Y. Huang, Electrochemical sensor using NH<sub>2</sub>-MIL-88(Fe)-rGO composite for trace Cd<sup>2+</sup>, Pb<sup>2+</sup>, and Cu<sup>2+</sup> detection, *J. Electroanal. Chem.*, 2017, **807**, 253–260.
- 40 H. Guo, Z. Zheng, Y. Zhang, H. Lin and Q. Xu, Highly selective detection of Pb<sup>2+</sup> by a nanoscale Ni-based metal-organic framework fabricated through one-pot hydrothermal reaction, *Sens. Actuators, B*, 2017, **248**, 430–436.

